

Development and understanding of $\text{La}_{0.85}\text{Sr}_{0.15}\text{Cr}_{1-x}\text{Ni}_x\text{O}_{3-\delta}$ anodes for $\text{La}_{5.6}\text{WO}_{11.4-\delta}$ -based Proton Conducting Solid Oxide Fuel Cells



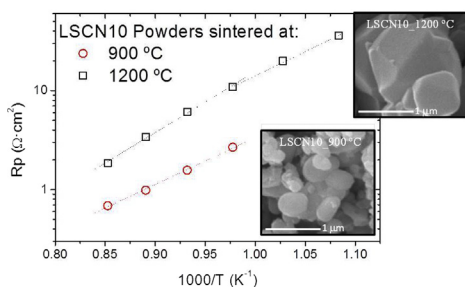
Cecilia Solís, Laura Navarrete, María Balaguer, José M. Serra*

Instituto de Tecnología Química, Universidad Politécnica de Valencia – Consejo Superior de Investigaciones Científicas, Avenida de los Naranjos s/n., 46022 Valencia, Spain

HIGHLIGHTS

- $\text{La}_{0.85}\text{Sr}_{0.15}\text{Cr}_{1-x}\text{Ni}_x\text{O}_{3-\delta}$ ($x = 0.1, 0.2$) is compatible with the protonic conductor $\text{La}_{5.6}\text{WO}_{11.4-\delta}$.
- The microstructure of anodes for proton conducting SOFC was optimized in symmetrical cells.
- Chromite anode performance improves with increasing Ni content.
- Decreasing the size of Ni nanoparticles improves anode performance.
- Langmuir–Hinshelwood mechanism describes the dissociative adsorption rate of H_2 .

GRAPHICAL ABSTRACT



ARTICLE INFO

Article history:

Received 11 October 2013

Received in revised form

23 January 2014

Accepted 4 February 2014

Available online 14 February 2014

Keywords:

SOFC anode

Chromite

Ni nanoparticles

Proton conductor

Lanthanum tungstate

ABSTRACT

Porous electrodes based on the system $\text{La}_{0.85}\text{Sr}_{0.15}\text{Cr}_{1-x}\text{Ni}_x\text{O}_{3-\delta}$ ($x = 0.1$ and 0.2) have been investigated as anodes for proton conducting solid oxide fuel cells based on the $\text{La}_{5.6}\text{WO}_{11.4-\delta}$ (LWO) electrolyte material. The microstructure of the anodes was optimized by varying both the starting powder morphology and the final anode sintering temperature. Two different electrode thicknesses were studied, i.e. 15 and 30 μm . The importance of the catalytic role of Ni was also studied by using different concentrations of Ni (10% and 20%) in the chromite and by tuning the Ni particle sizes through the control of the reduction temperature. Additionally, a ceramic–ceramic (cer–cer) composite electrode comprising a physical mixture of the optimized chromite and LWO phase was also considered. Finally, a kinetics study and modeling based on Langmuir–Hinshelwood mechanism was carried out in order to quantitatively describe the rate of dissociative adsorption of H_2 on the Ni particles spread on the chromite surface.

© 2014 Elsevier B.V. All rights reserved.

1. Introduction

The high protonic conductivity of the $\text{La}_{6-x}\text{WO}_y$ (LWO, with $0.4 < x < 0.7$) and its stability in CO_2 containing atmospheres make this material a promising candidate as electrolyte for proton

conducting solid oxide fuel cells (PC-SOFCs) [1–6]. Although this material exhibits mixed electronic–protonic conductivity under reducing conditions, its electronic conductivity is negligible when used as electrolyte subjected to a large $p\text{O}_2$ gradient (Air/ H_2), i.e. the cell voltage approaches the Nernst potential [7,8]. The increasing interest in these PC-SOFCs resides in the possibility of reducing the operation temperature and avoiding the fuel dilution. Therefore, new electrodes, both cathodes and anodes, compatible with LWO electrolyte are demanded.

* Corresponding author. Tel.: +34 963 879 448; fax: +34 963 877 809.

E-mail address: jmserra@itq.upv.es (J.M. Serra).

The high reactivity of the LWO phase with the widely used NiO [9] prioritizes the search of new anode materials compatible with LWO electrolyte. $\text{LaCrO}_{3-\delta}$ based materials have been broadly investigated as (i) interconnector for SOFC despite the extreme sensitivity to oxygen partial pressure and high manufacturing costs [10,11] and (ii) anode materials due to the redox stability and high ability to inhibit carbon coking [12,13] in CH_4 -fueled SOFCs. Indeed, Ni doped $\text{La}_{0.85}\text{Sr}_{0.15}\text{CrO}_{3-\delta}$ (LSC) has been tested as promising anode for conventional SOFC, since it combines sufficient electronic and oxygen-ion conductivity under anode operation conditions and catalytic activity by incorporating a catalyst in the electrode, e.g. ruthenium or nickel [14–16]. It has been reported that these Ni doped chromites split metallic Ni nanoparticles under reducing atmospheres and these catalytic particles enhance the anode performance [17]. Furthermore, chromites present mixed electronic and protonic conductivity in reducing atmospheres and they are compatible with LWO electrolyte phase, which make them promising anode materials for LWO based PC-SOFC [8,9]. Regarding the nature of the ionic transport through LWO electrolyte, at 900 °C the oxygen transport is twice the proton transport, although at lower temperatures (800 °C and below), proton transport is prevailing over oxygen ionic and electronic conduction. Indeed, the final application of this cell is in the temperature range below 800 °C [1,18].

The present work focuses on the study and optimization of $\text{La}_{0.85}\text{Sr}_{0.15}\text{Cr}_{1-x}\text{Ni}_x\text{O}_{3-\delta}$ (LSCN, with $x = 0.1$ and 0.2) as anode for LWO based PC-SOFCs. Firstly, the anode performance was improved by changing the microstructure of the electrode, i.e. by varying the sintering temperatures of both the starting powder and the screen printed porous electrode. The catalytic role of Ni was analyzed by incorporating different amounts of Ni in the chromite and by varying the Ni particles sizes (using different reducing temperatures). LSCN-LWO cer–cer composites were also studied by mixing the best chromite composition with the LWO protonic phase. Finally, a kinetics analysis based on Langmuir–Hinshelwood mechanism was carried out. The obtained model allowed describing the rate of dissociative adsorption of H_2 on the Ni particles spread on the chromite surface.

2. Experimental

$\text{La}_{0.85}\text{Sr}_{0.15}\text{Cr}_{0.9}\text{Ni}_{0.1}\text{O}_{3-\delta}$ (LSCN10) and $\text{La}_{0.85}\text{Sr}_{0.15}\text{Cr}_{0.8}\text{Ni}_{0.2}\text{O}_{3-\delta}$ (LSCN20) powders were prepared by citrate reaction route, and two different pre-sintering temperatures of the powders (1200 and 900 °C) were studied [17]. The $\text{La}_{5.5}\text{WO}_{11.25-\delta}$ used as protonic phase for the composite cathode was prepared by Pechini method [19] following the experimental procedure explained elsewhere [6]. Screen printing inks were prepared by mixing the ball-milled powders with a solution of ethylcellulose in terpineol (6%-wt.) and subsequently refined using a three roller mill (Exakt). $\text{La}_{5.6}\text{W}_{\text{O}11.4-\delta}$ (LWO) electrolyte powder was commercially provided by Cerptotech.

Crystalline phase of the different materials was characterized by X-ray diffraction (XRD) by a PANalytical Cubix X'Pert PRO diffractometer, using $\text{CuK}\alpha_{1,2}$ radiation and a X'Celerator detector in Bragg–Brentano geometry. XRD patterns were recorded in the 2θ range from 10° to 90° and analyzed using X'Pert Highscore Plus software.

Dense ~1 mm-thick LWO disks were obtained by uniaxially pressing the ball-milled LWO powder at ~120 MPa and final firing at 1500 °C for 5 h. Porous ~30 and 15 μm-thick electrodes were obtained by screen-printing the inks on both sides of LWO electrolyte disks. The standard electrode thickness was 30 μm. Firing temperature of the screen-printed anodes cells was 950, 1050, 1150 and 1250 °C for 2 h. Finally, the anodes were reduced at two

different temperatures, 900 and 800 °C. A summary of the different tested anodes (powder sintering temperature, anode sintering temperature and the final anode reduction temperature) is shown in Supporting Fig. 1. The final size of symmetrical cells was 15.5 mm in diameter, whereas anodes were ~9 mm in diameter.

LSCN/LWO/LSCN symmetrical cells were tested by electrochemical impedance spectroscopy (EIS) in two-point configuration. Input signal was 0 V DC – 20 mV AC in the 0.01–3 · 10⁵ Hz frequency range. This signal was generated by a Solartron 1470E and a 1455A FRA module equipment. EIS measurements were performed in the 900–650 °C range, under moistened atmospheres (2.5% vol. H_2O) at different $p\text{H}_2$ (by using fluxes of 100% H_2 and 50% and 5% of H_2 in He). Wet 5% D_2 in He (2.5% vol. D_2O) was also used in order to identify protonic processes expecting H/D isotopic effects. In all the cases, the total flow remained constant (100 mL min^{−1}). Raw impedance data were fitted to an equivalent circuit using Z-plot software.

The microstructure was investigated using scanning electron microscopy (SEM) (Zeiss Ultra 55), and elemental analysis was carried out with energy-dispersive X-ray spectroscopy (EDS) (INCA, Oxford). The porosity of the anodes was calculated by analyzing SEM images.

3. Results and discussion

3.1. Structural characterization of $\text{La}_{0.85}\text{Sr}_{0.15}\text{Cr}_{1-x}\text{Ni}_x\text{O}_{3-\delta}$ ($x = 0.1$ and 0.2) powders and compatibility with LWO material

XRD patterns of $\text{La}_{0.85}\text{Sr}_{0.15}\text{Cr}_{1-x}\text{Ni}_x\text{O}_{3-\delta}$ ($x = 0.1$ and 0.2) powders prepared by Pechini method and sintered at 900, 1050 and 1150 °C, are represented in Fig. 1a and b. It can be observed that at 900 °C, besides the chromite structure peaks, there is some amount of SrCrO_4 (diffraction peaks labeled with * in the graphs). These small traces of SrCrO_4 are in agreement with previously reported studies [20] and disappear when the sintering temperature is increased, i.e. above 1050 °C. No changes in cell parameter are induced through the sintering at higher temperatures, as inferred from the peaks position.

SEM images (Fig. 2) show grain size distribution of the different LSCN powders at two different magnifications (top and bottom). Important differences in the grain size distribution and their homogeneity are observed as a function of sintering temperature, i.e. the grains remain smaller and more homogenous when the powder is sintered at lower temperatures. LSCN10 sintered at 1200 °C (Fig. 2a) presents grains ranging from 800 nm to 1.6 μm, while LSCN10 sintered at 900 °C (Fig. 2b) shows a well distributed microstructure with grains of around 150 nm. These differences in the morphology of the powders affect the anode performance, as it will be discussed latter. When comparing different Ni-content powders, LSCN10 and LSCN20, both sintered at 900 °C, (Fig. 2b and c, respectively) no major differences in the grain morphology are observed although LSCN20 grain sizes are slightly smaller.

Chemical compatibility of LSCN10 and LSCN20 anode materials with LWO electrolyte was also tested at high temperature, imitating the electrode sintering process. Fig. 3 shows XRD patterns of a mixture of 50 vol.% of LSCN10 (sintered at 1200 °C) and LSCN20 (sintered at 900 °C) and 50 vol.% of LWO (sintered at 800 °C) before and after being commonly sintered in air at 1150 °C for 5 h. From the patterns it can be inferred that there is no reaction between the Ni-doped chromites, LSCN10 and LSCN20, and LWO since all diffraction peaks can be assigned to both chromite and LWO phases. The small changes in intensities and widths of the structural peaks are merely attributed to the different initial calcination temperature of each powder. Regarding the preparation of cer–cer composites, LSCN20 and LWO powders (SEM images showed in

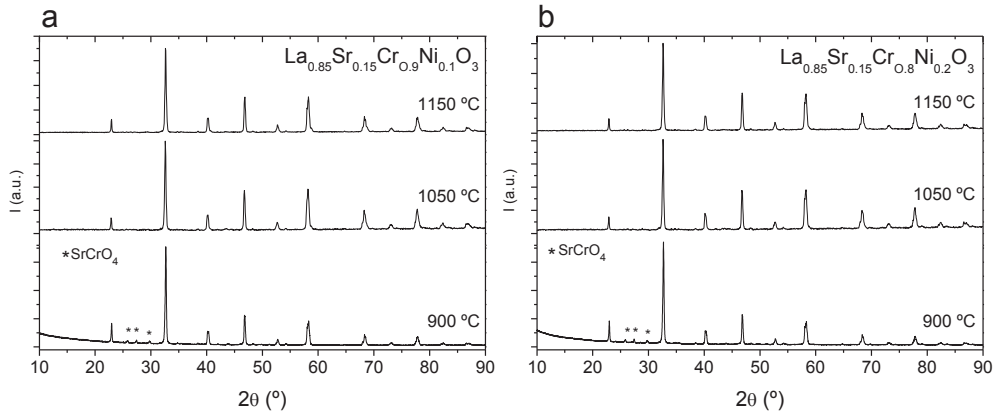


Fig. 1. XRD patterns of LSCN10 (a) and LSCN20 (b) powders sintered at 900, 1050 and 1150 °C.

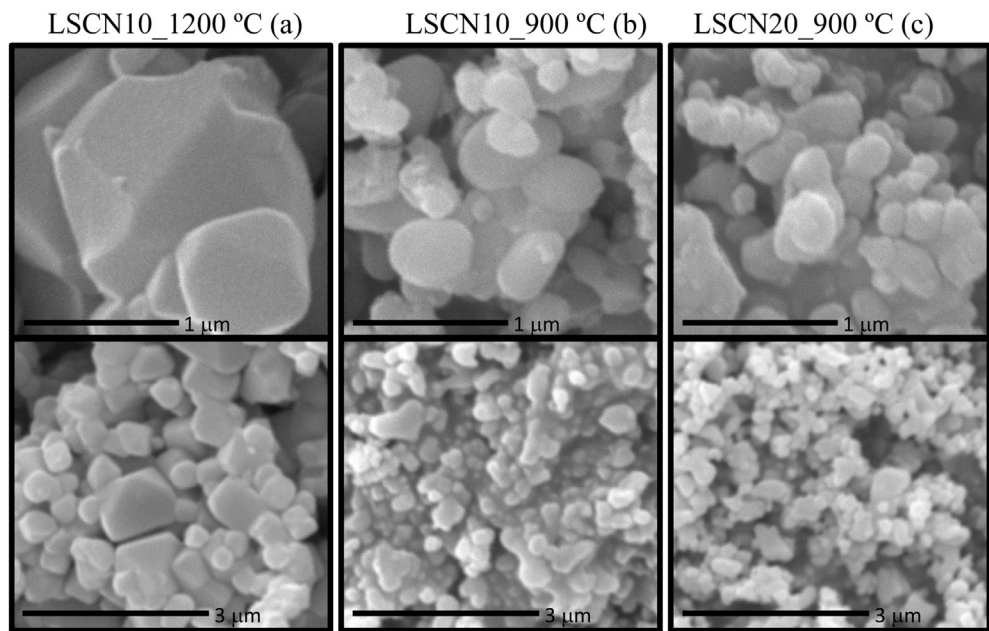


Fig. 2. SEM images of grain size distribution of LSCN10 sintered at 1200 °C (a) and 900 °C (b) and LSCN20 sintered at 900 °C (c).

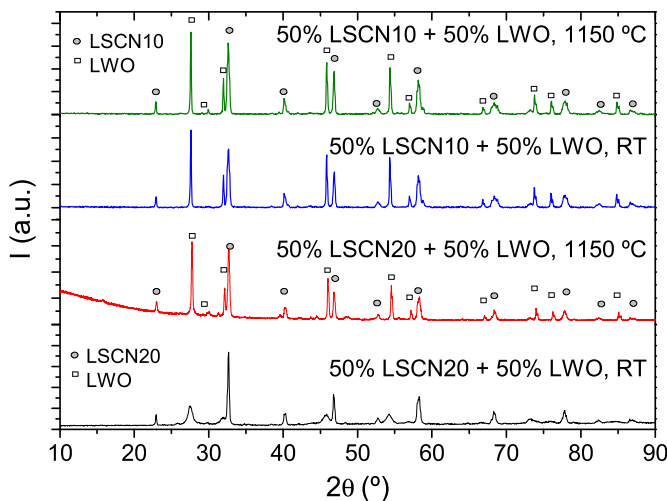


Fig. 3. XRD patterns of LSCN10 + LWO 50 vol.% and LSCN20 + LWO 50 vol.% after being mixed at RT and sintered together at 1150 °C for 5 h.

Supporting Fig. 2) have comparable grain sizes that allow the homogenous blending of the electrode.

LSCN10 and LSCN20 anodes sintered up to 1150 °C are stable and do not react with LWO electrolyte. However higher temperatures cause the formation of a thin reaction interface between the electrode and the electrolyte composed of a high concentration of big white particles, as can be seen in the SEM image of sample sintered at 1250 °C in Fig. 4. It is ascribed to a small reaction area between both materials due to the very high sintering temperature and the Ni content of the anode (it has been reported that NiO reacts with LWO [9,22,23]). For this reason, the highest selected temperature for anode sintering was 1150 °C. TEM analysis on FIB-lamellas of LSCN10 sintered at 1150 °C on LWO confirmed that no reaction or interdiffusion between both materials takes place [9].

The electrodes deposited on LWO-cells prepared with the same starting powder (LSCN10 pre-sintered at either 900 or 1200 °C) have a very similar microstructure and only differ in the degree of porosity, which decreases as the sintering temperatures rises (see SEM images in Fig. 4 and Supporting Fig. 3). Thus from Fig. 4 and by using computational image analysis, a porosity of 48%, 42% and 38%

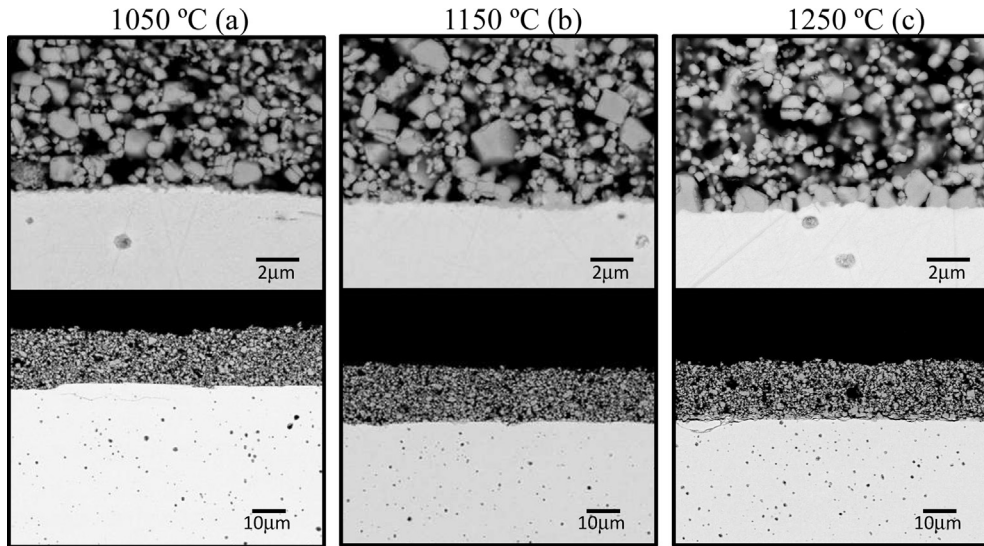


Fig. 4. SEM images of LSCN10/LWO/LSCN10 cross-sections of samples sintered at 1050, 1150 and 1250 °C. Starting LCN10 powder was pre-sintered at 1200 °C.

can be estimated for the samples sintered at 1050, 1150 and 1250 °C, respectively. A general summary of the samples prepared and the parameters considered in this study is provided in Supporting Information.

3.2. Electrochemical characterization of anodes based on single chromite

3.2.1. Effect of the starting powders morphology associated to the pre-sintering temperature

The effect of the sintering powder temperature is analyzed in terms of the polarization resistance (R_p). LSCN10 anodes sintered at 1150 °C and made of powders pre-sintered at 900 and 1200 °C are analyzed in Fig. 5a, by using 100% H_2 flow saturated with water.

The anode prepared using the powder pre-sintered at 900 °C, shows R_p values substantially lower than those obtained for the anode prepared with the powder pre-sintered at 1200 °C (with 4 times smaller R_p at 750 °C). The improved performance of the anode with the powder pre-sintered at 900 °C is ascribed to its microstructure (Fig. 2). Specifically, the smaller grain size of the powder pre-sintered at 900 °C (150 nm) results in higher surface area available for the H_2 oxidation partial reaction in contrast with the powder pre-sintered at 1200 °C, which present particles with grain sizes ranging from 0.8 to 1.6 μm .

Further understanding of the microstructure role on the anode operation can be achieved by means of the impedance spectroscopy analysis of symmetrical cells. Electrochemical impedance spectra recorded on anodes sintered at 1150 °C, performed in wet (2.5 vol.% H_2O) H_2 at 750 °C, are represented in Fig. 5b and c (Nyquist and Bode plots, respectively) after subtracting the electrolyte contribution. EIS modeling is carried out using the original raw data. EIS measurements can be fitted to a double $R||CPE$ circuit, as the one showed in Fig. 6a, more or less overlapped, occurring at different characteristic frequencies, low frequencies (LF, 5–100 Hz) and medium frequencies (MF, 0.5–26 kHz). An example of the obtained fittings, previous to the electrolyte subtraction, is plotted in Fig. 6b. The open symbols correspond to experimental data and the lines correspond to the fitted model. Table 1 summarizes the obtained fitting parameters for the different electrodes measured in this work (extended parameter are showed in Supporting Fig. 4). R_0 corresponds to the ohmic resistance of the whole cell including the electrolyte and current

collectors and L to the inductance of the wires. In this context, R_p is the sum of R_1 and R_2 . In the rest of Nyquist and Bode plots R_0 and L contributions have been removed to facilitate the direct comparison among different anodes, as they only correspond to the electrolyte material and to the wire, respectively. Note that the two anodes made of powder pre-sintered at 900 °C and sintered at 1050 and 950 °C only present values for the LF circuit as the MF arc was negligible in these cases.

From the raw impedance spectra and the fitting parameters (Table 1), it can be inferred that the electrochemical performance of the anodes is principally limited by the LF associated processes which are mainly related to surface associated reactions [9,22]. In

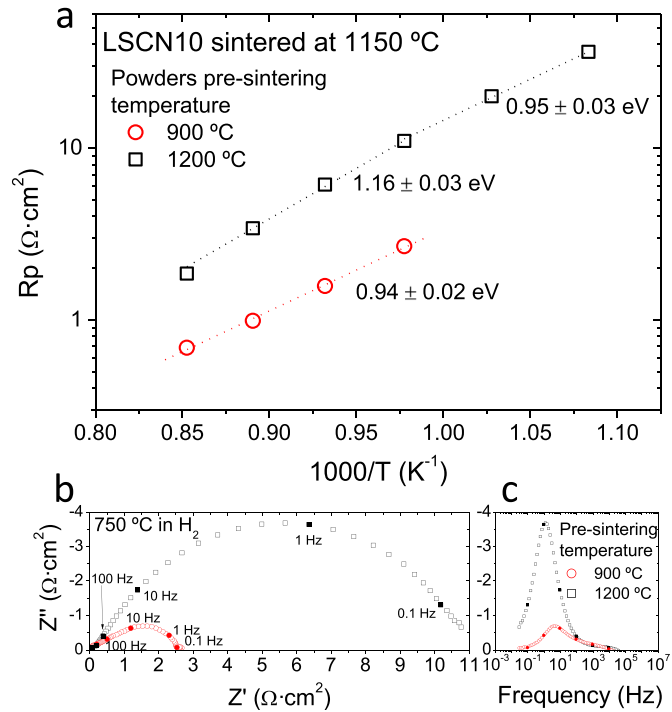


Fig. 5. R_p of LSCN10 anodes sintered at 1150 °C made from powder calcined at 900 °C and 1150 °C (a) and impedance spectra at 750 °C Nyquist (b) and Bode (c) plots.

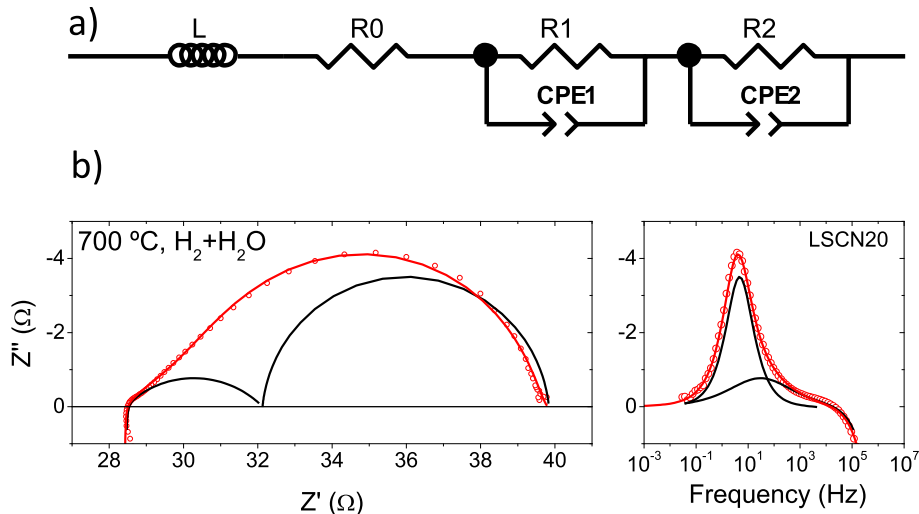


Fig. 6. Equivalent circuit model used for the EIS measurements (a) and obtained fittings (lines) to the LSCN20 experimental data (open symbols) (b).

agreement with this, the better performance of the LSCN10 anode with powder pre-sintered at 900 °C is ascribed to its higher active surface area which enhances surface kinetic limited process, reducing LF resistance [9,22].

3.2.2. Effect of the final anode sintering temperature

Since the powder pre-sintered at 900 °C exhibits the most appropriate microstructure for anode operation, this pre-sintering temperature was selected for preparing the symmetrical cells for

Table 1

Summary of the fitting parameters for the different experimental data of the tested anodes to the equivalent circuit showed in Fig. 6a.

Sample	T °C	R0 Ω	R1 Ω	C1 F	Freq1 Hz	R2 Ω	C2 F	Freq2 Hz
LSCN10				LF	LF	MF	MF	MF
Powder pre-sintered at 1200 °C								
Anode sintered at 1150 °C 100% H ₂	900	10.85	5.84	6.4E-03	26.6			
	850	14.13	10.62	5.4E-03	17.5			
	800	18.75	18.92	4.6E-03	11.6	0.31	2.2E-04	14651.5
	750	25.7	33.86	3.9E-03	7.6	0.65	1.5E-04	10415.7
	700	34.76	58.59	3.5E-03	4.9	4.16	9.4E-05	2548.3
	650	47.81	103.60	3.1E-03	3.1	10.11	1.9E-04	512.8
Powder pre-sintered at 900 °C								
Anode sintered at 1150 °C 100% H ₂	900	10.25	1.82	6.2E-03	88.7	0.21	2.6E-04	18525.5
	850	13.42	2.49	5.8E-03	69.0	0.47	5.6E-04	3789.5
	800	18.05	3.95	5.2E-03	48.4	0.86	3.1E-04	3717.4
	750	27.48	6.12	5.4E-03	30.4	2.08	2.0E-04	2422.9
Anode sintered at 1100 °C 100% H ₂	900	10.46	3.43	2.8E-03	102.8			
	850	13.83	5.26	2.1E-03	89.3	0.11	3.8E-04	24302.1
	800	18.39	8.51	2.0E-03	60.2	0.37	3.6E-04	7452.9
	750	24.9	13.91	2.0E-03	36.7	1.38	2.2E-04	3363.4
	700	32.73	20.62	2.1E-03	23.1	2.91	2.7E-04	1282.0
	650	42.81	33.66	2.5E-03	11.7	8.64	2.5E-04	472.5
Anode sintered at 1050 °C 100% H ₂	900	10.19	16.48	9.9E-03	6			
	850	13.53	20.91	5.7E-03	8			
	800	18.23	27.64	3.8E-03	9			
	750	25.37	45.67	2.9E-03	7			
	700	35.43	72.31	2.3E-03	6			
Anode sintered at 950 °C 100% H ₂	900	9.273	7.92	4.1E-03	33.2			
	850	11.94	12.95	2.4E-03	32.8			
	800	16.03	22.46	1.7E-03	26.6			
	750	21.78	39.18	1.2E-03	20.7			
	700	29.45	69.75	1.0E-03	14.3			
	650	36.97	137.60	8.1E-04	8.9			
LSCN20								
Anode sintered at 1150 °C 100% H ₂	750	15.34	3.37	3.7E-03	80.3	0.56	6.8E-05	26086.9
	700	20.45	5.24	3.8E-03	49.7	1.48	2.2E-04	3104.1
	650	28.34	8.84	4.4E-03	25.8	2.56	7.4E-04	529.9
	600	38.19	15.94	4.4E-03	14.4	4.57	4.5E-04	489.8

the rest of this study. Therefore, in the next, sintering temperatures only refer to the final anode sintering.

Fig. 7a collects the R_p (in wet hydrogen) of LSCN10 symmetrical cells sintered at 950, 1050, 1100 and 1150 °C as a function of inverse temperature. The lowest R_p is achieved for the sample sintered at 1150 °C and the highest one corresponds to the one sintered at 1050 °C. In order to highlight this aspect, **Fig. 7b** illustrates how the electrochemical performance, i.e. R_p at 750 °C, depends on the final electrode sintering temperature. The anode performance does not improve R_p significantly up to 1050 °C, but a continuous improvement can be observed beyond it. The best performance shown by the anode sintered at 1150 °C can be related to a better connectivity among the particles while keeping the extended electrode surface, i.e. no major particle coarsening occurs, as deduced from SEM analysis (**Supporting Fig. 3**).

Fig. 7c and d depict the impedance spectra (Nyquist and Bode plots, respectively) at 750 °C of the LSCN10 anodes sintered at these four different temperatures (modeling results are shown in **Table 1**). In all the cases, the anode operation is principally limited by LF processes. These LF processes show characteristic frequencies at the range 1–100 Hz and associated capacitances of $5 \times 10^{-3} - 2 \times 10^{-2} \text{ F cm}^{-2}$ that are typically related to dissociation adsorption or surface diffusion reactions [9,22] and not to gas diffusion processes [[23] page 259]. The MF contribution shows higher characteristic frequencies (0.5–25 kHz) and the associated capacitances of $10^{-4} - 10^{-3} \text{ F cm}^{-2}$ that can be interpreted as surface exchange coupled with bulk ionic transport in mixed conducting electrodes [22,24,25].

On the other hand, as the overall R_p decreases, the limiting processes shift to higher frequencies. This fact suggests that the anode sintering at high temperatures improves the limiting LF processes albeit the specific surface area of the electrode decreases with rising temperature. This improvement is ascribed to the aforementioned better connectivity among anode particles, which

in these mixed conducting electrodes is coupled to surface reaction/processes of dissociation adsorption and surface diffusion of hydrogen (as the material conducts both electrons and protons) and appears at LF in EIS analysis [26,27].

3.2.3. Effect of the Ni content

Under anode operation conditions (wet hydrogen above 650 °C) LSCN is reduced and metallic Ni nanoparticles precipitate on the surface of the chromite grains [9,17,28,29]. The presence of these Ni nanoparticles on the surface gives rise to the formation of structural defects [17,30] and metallic Ni, which increases substantially the catalytic activity towards H₂ evolution with respect to the LSC anode material. Nevertheless, the TEM analysis of this La_{0.85}Sr_{0.15}Cr_{0.9}Ni_{0.1}O_{3-δ} reveals (**Supporting Fig. 5**) that a higher amount of Ni would be needed for a complete coverage of LSCN grain surface.

The influence of the Ni content on the anode performance was analyzed by comparing chromite anodes with 10% and 20% of Ni (LSCN10 and LSCN20, respectively). For this comparison LSCN20 anodes were prepared from the 900 °C pre-sintered powders, which are compatible with and of similar microstructure than the LWO electrolyte (as demonstrated in **Figs. 2** and **3**). The Ni nanoparticles formed on the anode upon reduction at 900 °C have sizes of $19.7 \pm 3 \text{ nm}$ and $19.5 \pm 5 \text{ nm}$ for LSCN10 and LSCN20, respectively (**Supporting Fig. 5**).

R_p of the LSCN10 and LSCN20 symmetrical cells sintered at 1150 °C are represented as a function of inverse temperature in **Fig. 8a**. R_p of the pure LSC is also depicted, for comparison. The introduction of Ni improves remarkably the anode performance and the best performance of LSCN20 anode can be attributed to the higher Ni content, which promotes surface processes due to its higher catalytic activity. EIS analysis of both LSCN10 and LSCN20 symmetrical cells shown in **Fig. 8b** and c (Nyquist and Bode plots, respectively) reveals that this performance improvement can be

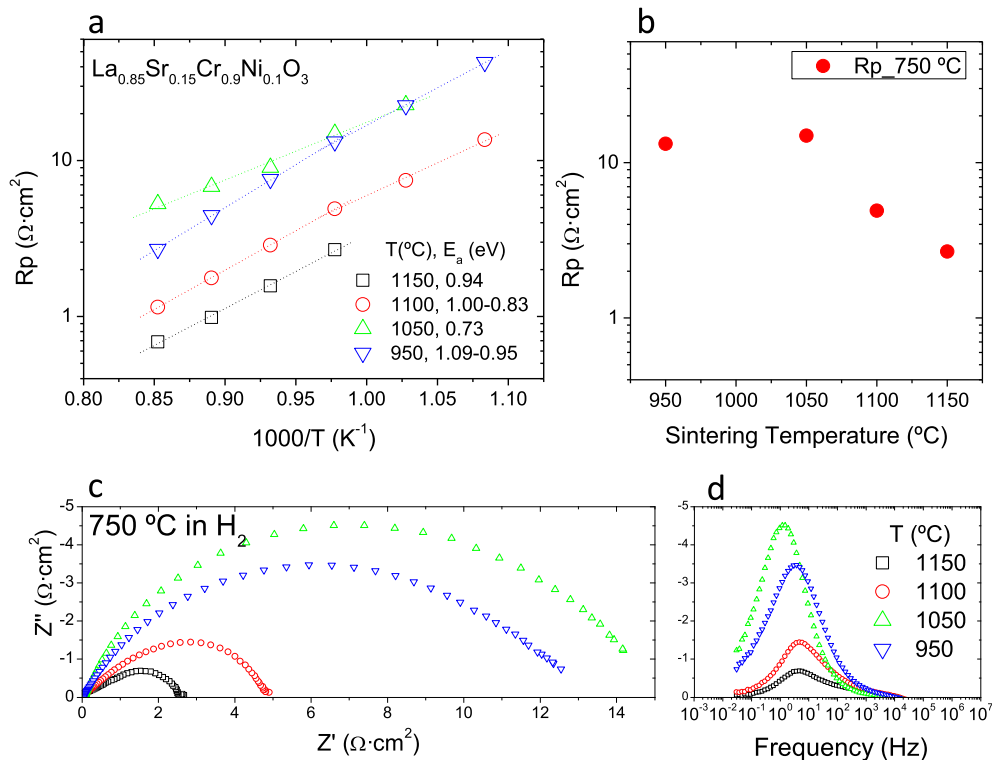


Fig. 7. R_p as a function of temperature of the LSCN10 anodes sintered at different temperatures (a), R_p at 750 °C as a function of sintering temperature (b) and EIS in wet H₂ of the different symmetrical cells, Nyquist (c) and Bode (d) plots.

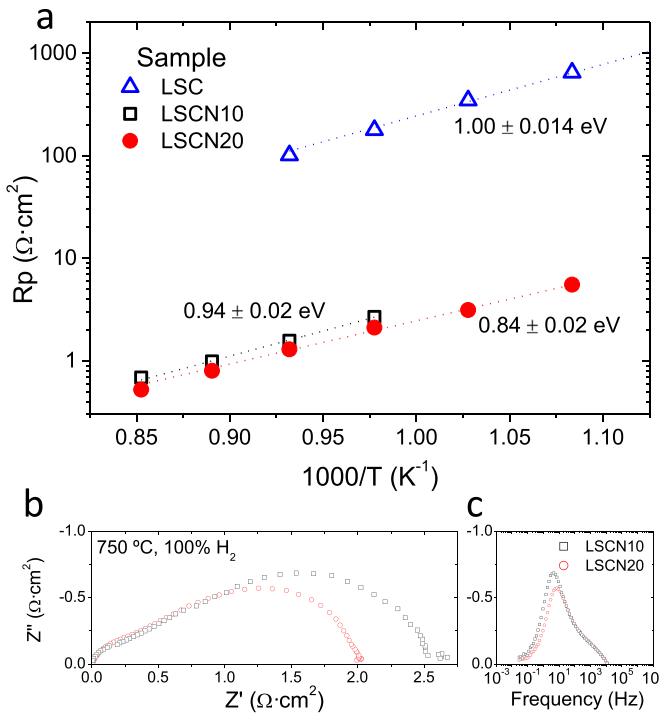


Fig. 8. Rp of symmetrical cells with LSC, LSCN10 and LSCN20 anodes sintered at 1150 °C (a) and impedance spectra of LSCN10 and LSCN20 measured in wet H₂ at 750 °C, Nyquist (b) and Bode (c) plots.

directly ascribed to a decrease in the contributions of LF associated processes. In fact, LF resistances decrease almost 3 times as can be seen in the Table 1. This is in line with the catalytic role of the Ni and the higher surface concentration of Ni in the LSCN20 anode, as expected and observed in previous works by temperature-programmed reduction experiments (TPR) measurements (Supporting Fig. 5c) [9,17].

3.2.4. Effect of reduction temperature and anode thickness

Once observed the importance of the catalytic activity of Ni nanoparticles, this section studies how the Ni morphology can be varied by using different reduction temperatures. In parallel, the anode thickness is studied. As deduced from TEM analysis of chromite powder, [17] by changing the anode reduction temperature from 900 to 800 °C, Ni particle size decreases from 19.7 ± 3 nm to 16.0 ± 2.6 nm, respectively. The observed effect of the reduction temperature on the precipitated metal crystallite size is in line with previous studies on perovskites [31]. This two reducing temperatures were applied on anodes with 15 and 30 μm thickness made of LSCN20.

Fig. 9a depicts the achieved Rp for four LSCN20 symmetrical cells, sintered at 1150 °C in air, where the total thickness and the reduction temperature have been changed: 30 μm and 15 μm (squared and round symbols, respectively) and both reduced at 900 °C and 800 °C (open and solid symbols, respectively). The influence of the reduction temperature on the electrochemical performance is much more important than the magnitude of the electrode thickness. Namely, Rp decreases four times for the materials reduced at 800 °C. EIS spectra represented in Fig. 9b and c (measurements in wet H₂ at 750 °C) show that the anode improvement is again principally associated with a decrease in the LF processes, likely related to surface kinetics reaction. This could be attributed to the slightly smaller size of Ni nanoparticles obtained upon reduction at 800 °C (16 nm) that gives rise to a higher

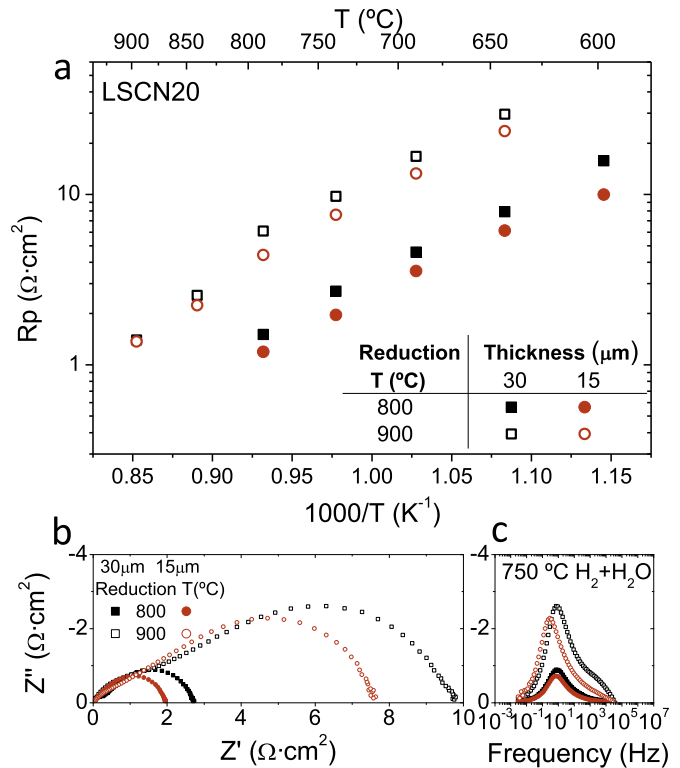


Fig. 9. Rp of LSCN20 anodes (sintered at 1150 °C) of 30 and 15 μm thickness and both reduced at 900 and 800 °C (a) and their impedance spectra at 750 °C in wet H₂, Nyquist (b) and Bode (c) plots.

catalytic active surface area, compared to that created by the Ni particles formed at 900 °C (of around 20 nm). TPR measurements of LSCN20 revealed that the amount of Ni segregated in the materials treated at 800 °C and 900 °C is the same, since no hydrogen consumption is detected at temperatures above 500 °C [17]. Irrespective of the reduction temperature, the optimum thickness is 15 μm, although the Rp variation with thickness is very small with regard to that produced by changing Ni particle sizes.

3.3. LSCN20/LWO cer–cer anode characterization

A common practice for improving the electrode performance in protonic fuel cells is the incorporation of a certain amount of the electrolyte material in the electrode composition, as it implies the introduction of proton conducting pathways in the electrode and better matching of thermal expansion between electrode and electrolyte [32–37]. Fig. 10a illustrates the Rp of LSCN20 anode and the cer–cer made when 40 vol.% of LWO phase is introduced. A huge increase in the Rp is observed with the introduction of the LWO phase. This increase could be related to a mere dilution effect, specifically, due to (1) the chromite in these conditions is not limited by the protonic conductivity for the anode operation [9]; (2) the decrease in the catalytic activity and (3) the reduction of the electrical conductivity when LWO is introduced. Fig. 10b shows the Rp evolution as a function of the amount of the LWO phase incorporated into the LSCN20 anode, which confirms a continuous increase of Rp with the addition of the LWO phase.

EIS measurements at 750 °C of LSCN20 and LSCN20/LWO 60/40 anodes are compared in Fig. 10c and d (Nyquist and Bode plots). The smaller LF arc of the LSCN20 anode attributes its improved performance to its higher catalytic activity. In addition, the appearance of the HF arc can be related to the decrease of total conductivity of the composite anode. In fact, the addition of the LWO phase

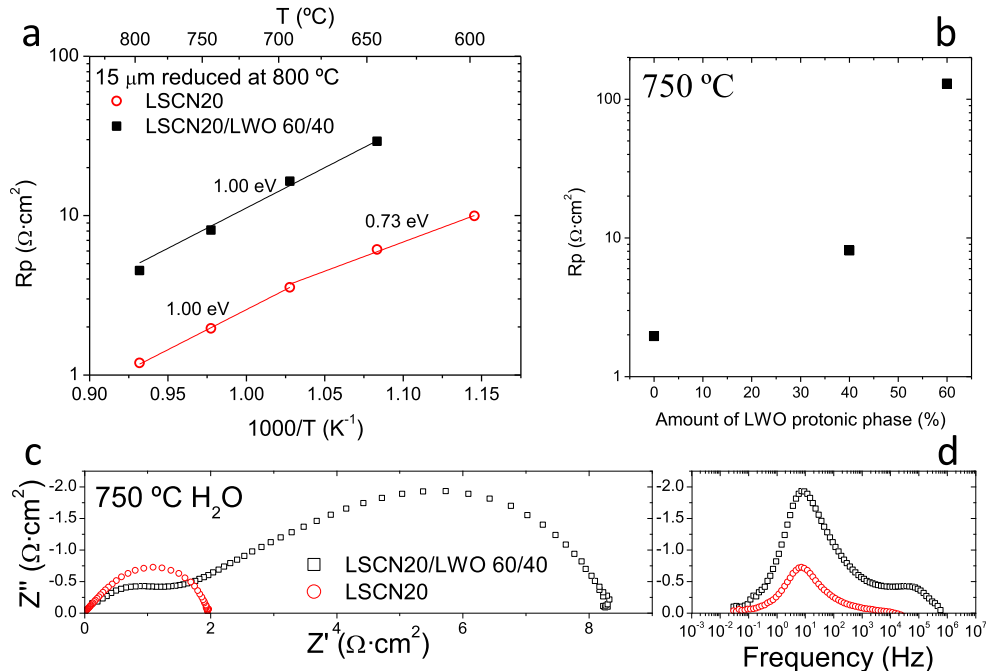


Fig. 10. Rp of LSCN20/LWO 60/40 vol.% anode sintered at 1150 °C compared to single LSCN20 electrode (a), Rp at 750 °C in 100% H₂ as a function of the introduced amount of LWO prototypic phase into the LSCN20 anode (b) and EIS measurements, Nyquist (c) and Bode (d) plots, in wet H₂ of symmetrical cells of LSCN20 and LSCN20/LWO 60/40 cer–cer anodes (15 μm of thickness) sintered at 1150 °C and reduced at 800 °C.

decreases the total conductivity of the anode by considering a mere dilution effect of the electron conducting phase and this could give rise to the loss of electronic percolation pathways.

3.4. Kinetics modeling

The electrochemical behavior of these chromite anodes is principally limited by LF processes in all the measured conditions. As these processes seem to be related to dissociative adsorption or surface diffusion of hydrogen, the inverse of the LF resistance (R_{LF}) can be assumed to be proportional to the rate of dissociative adsorption of H₂. There are different mechanisms by which a molecule or atom adsorb onto a substrate surface and reacts. Langmuir–Hinshelwood mechanism follows:

1. Adsorption from the gas-phase
2. Desorption to the gas-phase
3. Dissociation of molecules at the surface
4. Reactions between adsorbed molecules

While Eley-Rideal mechanism has another step:

5. Reactions between gas and adsorbed molecules

In the case of dissociative adsorption of H₂ only Langmuir–Hinshelwood mechanism takes place. Therefore, the rate of a heterogeneous reaction is controlled by the reaction of the adsorbed molecules being adsorption and desorption pressures in equilibrium. Langmuir adsorption equation relates the adsorption of molecules on a solid surface with gas pressure above the solid surface at a fixed temperature:

$$\theta = \frac{K \cdot P}{1 + K \cdot P} \quad (1)$$

where θ is the fractional coverage of the surface, P is the gas pressure (or concentration) and K the adsorption constant.

Langmuir equation assumes that all active sites on the solid surface are equal and have equal affinity for adsorbate molecules. In the present anodes, these active sites are the Ni nanoclusters segregated on the surface of the chromite, therefore they are independent of the chromite properties. For unimolecular reactions ($A_{\text{gas}} \leftrightarrow A_{\text{ads}}$) in which the decomposition occurs uniformly along the surface where the rate determining step (rds) is the surface decomposition $r = k\theta$ (k is a rate constant), r can be written as:

$$r = k \frac{K \cdot P}{1 + K \cdot P} \quad (2)$$

On the other hand, for a bimolecular reaction, and specifically for the dissociative adsorption of H₂, two adjacent adsorption sites (*) are needed and then

$$H_2 + 2^* \leftrightarrow 2H^* \quad (3)$$

$$\theta = \frac{(K_{H_2} \cdot P_{H_2})^{0.5}}{1 + (K_{H_2} \cdot P_{H_2})^{0.5}} \quad (4)$$

$$r = k\theta_H\theta_H = k \frac{K_{H_2} \cdot P_{H_2}}{\left(1 + (K_{H_2} \cdot P_{H_2})^{0.5}\right)^2} \sqrt{b^2 - 4ac} \quad (5)$$

In the studied anodes (where LF surface processes limit Rp) the rate of dissociative adsorption of H₂ is proportional to $1/R_{LF}$ and then:

$$\frac{1}{R_{LF}} \propto r = k \frac{K \cdot P_{H_2}}{\left(1 + \sqrt{K \cdot P_{H_2}}\right)^2} \quad (6)$$

Two limiting steps can be distinguished. At low pressures $\sqrt{K \cdot P_{H_2}} <> 1$ (weak binding) and then $r \rightarrow k \cdot K_{H_2} \cdot P_{H_2}$, so the reaction rate is linear with pH₂. At high pressures $\sqrt{K \cdot P_{H_2}} >> 1$ (strong binding) $r \rightarrow k$, so is independent on pH₂ and tends to the rate constant value. This rate constant k is proportional to the number of

the active sites (surface area and metal dispersion) and the size/shape of the catalyst clusters.

When $1/R_{LF}$ is represented as function of the pH_2 , as illustrated in Fig. 11a for LSCN10 and LSCN20 anodes sintered at 1150 °C, the fits to equation (6) gives K constant and a coefficient proportional to k measured in $\Omega^{-1} \text{cm}^{-2}$.

Fig. 11b displays k and K coefficients as a function of the temperature of LSCN20 and LSCN20/LWO 60/40 cer–cer anodes. The addition of the LWO prototypic phase into the LSCN20 anode decreases the rate constant k , as corresponds to the material with reduced concentration of active sites (Ni clusters). However the intrinsic catalytic activity of the sites should not be modified, and therefore the activation energy derived from k should not change, as it is confirmed in the graph. The absorption constant K of both electrodes is very similar as an inherent material property of Ni sites on LSCN grains.

Actually, at 750 °C K is almost constant or slightly decreases with anode sintering temperature. However there is a huge improvement of rate constant k with anode sintering temperature (see Supporting Fig. 6) that dominates the total performance of the anode. Furthermore it is also slightly higher for LSCN20 sample, as corresponds to its proportionality to the active sites which are the active Ni nanoparticles in this case.

Summarizing, as LSCN10 and LSCN20 samples present surface limiting processes, Langmuir–Hinshelwood mechanism was proposed for describing their rate of dissociative adsorption of H_2 , that

is proportional to $1/R_{LF}$. Adsorption and rate related constants were calculated and compared for different samples. Rate constant increases with the rise of anode sintering temperature, which agrees with the total improvement of the anode with the sintering temperature. This could be assigned to a better connectivity among particles while the anode surface area does not change noticeably. In fact, a negative effect in the rate would be expected if a substantial reduction in the surface area was achieved. However, in the present case, the low sintering activity of the chromite prevents the particle coarsening and the loss of surface area. Furthermore, the increase in Ni concentration in the anode composition induces a slight increase in the rate constant, ascribed to the presence of higher amount of active sites.

This model describes uniquely the surface mechanism related to hydrogen dissociation and proton formation, which is assumed to be the rate limiting in this electrodes. Consequently, this model does not provide information about the further transport of the proton towards and through the LWO electrolyte.

4. Conclusion

Different anodes based on Ni doped LaCrO_3 were analyzed in this study by means of EIS measurements. First the compatibility of $\text{La}_{0.85}\text{Sr}_{0.15}\text{Cr}_{0.9}\text{Ni}_{0.1}\text{O}_{3-\delta}$ and $\text{La}_{0.85}\text{Sr}_{0.15}\text{Cr}_{0.8}\text{Ni}_{0.2}\text{O}_{3-\delta}$ with $\text{La}_{5.6}\text{W}_{11.4-\delta}$ electrolytes was confirmed as no reaction between materials was found by XRD measurements.

Symmetrical cells based on the single materials were prepared at different temperatures and also with powder pre-sintered at different temperatures, inferring information about the best microstructure for the anode operation. Thus R_p drops from 10.97 to 2.68 $\Omega \text{ cm}^2$ at 750 °C when the pre-sintering temperature of the LSCN10 powder is reduced from 1200 to 900 °C, and thus smaller grains, involving higher surface area, are obtained.

The catalytic role of Ni was studied (1) by comparing the behavior of similar symmetrical cells with different Ni content (10% and 20%), and (2) by changing Ni particle sizes by using different reducing temperatures. Thus, at 750 °C, R_p is reduced from the 188 $\Omega \text{ cm}^2$ of the pure LSC (with no Ni) to 2.68 $\Omega \text{ cm}^2$ when 10% of Ni is introduced (LSCN10) and finally to 2.11 $\Omega \text{ cm}^2$ when the amount of Ni is increased up to 20% (LSCN20). When Ni nanoparticles size drops from 20 to 16 nm R_p diminishes from 7.58 to 2.11 $\Omega \text{ cm}^2$ (studied in samples with the same amount of Ni, LSCN20). These facts evidence the importance of the catalytic activity of Ni that helps anode performance by reducing surface (low frequency associated) related processes.

Finally, as low frequency surface related processes limit the performance of these anodes, Langmuir–Hinshelwood mechanism was proposed for describing their rate of dissociative adsorption of H_2 , which is proportional to $1/R_{LF}$. Rate and adsorption related constants were calculated and compared. The increase of the rate constant with the anode sintering temperature and with the higher amount of Ni agree with the improvement of the anode due to the better connectivity of particles and with the higher amount of Ni that increases the active sites of the anode. Very slight changes were observed for adsorption constants, as corresponds to an intrinsic property of the Ni active nanoparticles.

Acknowledgments

Funding from the Spanish Government (ENE2011-24761, SEV-2012-0267, BES-2012-053180) and European Union (FP7 Project EFFIPRO – Grant Agreement 227560) are kindly acknowledged. Authors are indebted to M. Fabuel for sample preparation and Forschungszentrum Jülich (Dr. M. Ivanova) for SEM analysis.

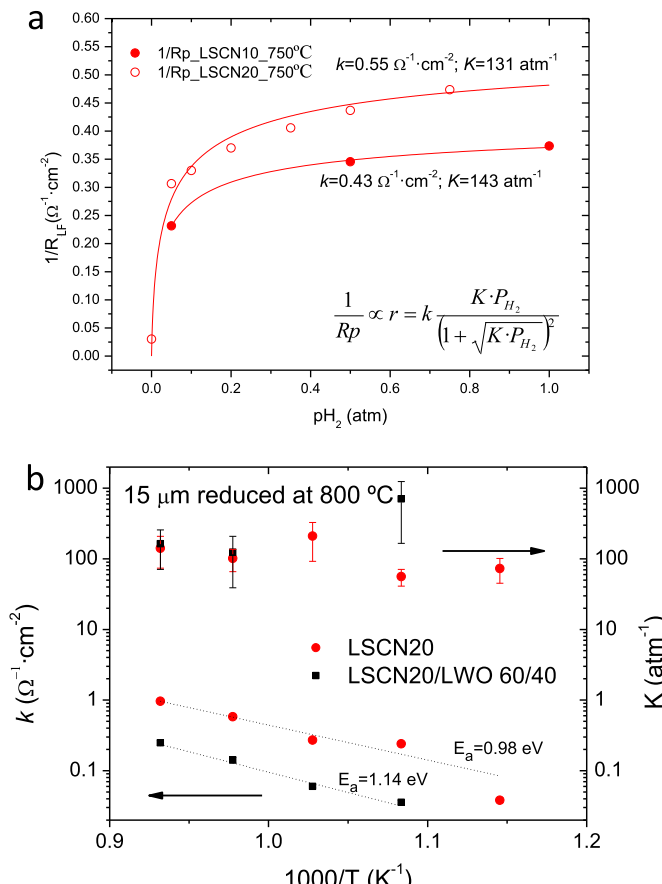


Fig. 11. $1/R_p$ as a function of pH_2 for LSCN10 and LSCN20 anodes sintered at 1150 °C (a) and calculated k and K parameters, proportional to rate and adsorption constants respectively, as a function of inverse temperature for LSCN20/LWO cer–cer anode compared to LSCN20 anode (b).

Appendix A. Supplementary data

Supplementary data related to this article can be found at <http://dx.doi.org/10.1016/j.jpowsour.2014.02.015>.

References

- [1] R. Haugsrud, C. Kjølseth, *J. Phys. Chem. Solids* 69 (2008) 1758–1765.
- [2] C. Solís, S. Escolástico, R. Haugsrud, J.M. Serra, *J. Phys. Chem. C* 115 (2011) 11124–11131.
- [3] A. Magraso, J.M. Polfus, C. Frontera, J. Canales-Vazquez, L. Kalland, C.H. Hervoches, S. Erdal, R. Hancke, S.S. Islam, T. Norby, R. Haugsrud, *J. Mater. Chem.* 22 (2012) 1762–1764.
- [4] J.M. Serra, S. Escolástico, M. Balaguer, W.A. Meulenberg, H.P. Buchkremer, T. Scherb, G. Schumacher, M.W. Lumey, R. Dronskowski, Ceramic hydrogen-permeable membranes made of mixed proton-electronic conducting materials based on the system Ln₆WO₁₂, in: Proceedings of 2009 E-MRS Fall Meeting, September 14–18, Warsaw, p. 140.
- [5] S. Escolástico, C. Solís, J.M. Serra, *Int. J. Hydrogen Energy* 36 (2011) 11946–11954.
- [6] S. Escolástico, V.B. Vert, J.M. Serra, *Chem. Mater.* 21 (2009) 3079–3089.
- [7] C. Solís, L. Navarrete, S. Roitsch, J.M. Serra, *J. Mater. Chem.* 22 (2012) 16051–16059.
- [8] S. Julsrud and B. Vigeland, Norsk Hydro ASA, International Publication Number: WO 03/0307490 A1 Solid Multicomponent Mixed Proton and Electron Conducting Membrane, Priority Date 30/10/2001.
- [9] C. Solís, V.B. Vert, M. Balaguer, S. Escolástico, S. Roitsch, J.M. Serra, *ChemSusChem* 5 (2012) 2155–2158.
- [10] W.Z. Zhu, S.C. Deevi, *Mater. Sci. Eng. A* 348 (2003) 227–243.
- [11] J.W. Fergus, *Mater. Sci. Eng., A* 397 (2005) 271–283.
- [12] X. Zhi, Q. Zhong, X. Zhao, H. Yan, *Appl. Surf. Sci.* 257 (2011) 1967–1971.
- [13] S. Primdahl, J.R. Hansen, L. Grahl-Madsen, P.H. Larsen, *J. Electrochem. Soc.* 148 (2001) A74–A81.
- [14] J. Sfeir, *J. Power Sources* 118 (2003) 276–285.
- [15] A.L. Sauvet, J.T.S. Irvine, *Solid State Ionics* 167 (2004) 1–8.
- [16] S. Li, S. Wang, Y. Wang, H. Nie, T.L. Wen, *Fuel Cells* 6 (2006) 451–454.
- [17] V.B. Vert, F.V. Melo, L. Navarrete, J.M. Serra, *Appl. Catal. B: Environ.* 115–116 (2012) 346–356.
- [18] R. Hancke, A. Magraso, T. Norby, R. Haugsrud, *Solid State Ionics* 231 (2013) 25–29.
- [19] M.P. Pechini, Patent Number: US 3330697, 1967.
- [20] X. Ding, Y. Liu, L. Gao, L. Guo, *J. Alloys Compd.* 458 (2008) 346–350.
- [22] M. Balaguer, C. Solís, F. Bozza, N. Bonanos, J.M. Serra, *J. Mater. Chem. A* 1 (2013) 3004–3007.
- [23] C. Solís, M. Balaguer, F. Bozza, N. Bonanos, J.M. Serra, *Appl. Catal. B: Environ.* 147 (2014) 203–207.
- [24] E. Barsoukov, J.R.I. Macdonald, *Impedance Spectroscopy Theory, Experiment, and Applications*, John Wiley & Sons, 2005.
- [25] J.M. Serra, V.B. Vert, *J. Electrochem. Soc.* 157 (2010) B1349–B1357.
- [26] M. González-Cuenca, W. Zipprich, B.A. Boukamp, G. Pudmich, F. Tietz, *Fuel Cells* 1 (2001) 3–4.
- [27] V.B. Vert, J.M. Serra, *Fuel Cells* 5 (2009) 663–678.
- [28] J. Sfeir, P.A. Buffet, P. Möcli, N. Xanthopoulos, R. Vasquez, H.J. Mathieu, J. Van Herle, K.R. Thampi, *J. Catal.* 202 (2001) 229–244.
- [29] W. Kobsiriphat, B.D. Madsen, Y. Wang, M. Slah, L.D. Marks, S.A. Barnett, *J. Electrochem. Soc.* 157 (2010) B279.
- [30] M. Oishi, K. Yashiro, J.-O. Hong, Y. Nigara, T. Kawada, J. Mizusaki, *Solid State Ionics* 178 (2007) 307–312.
- [31] W. Kobsiriphat, B.D. Madsen, Y. Wang, L.L. Marks, S.A. Barnett, *Solid State Ionics* 180 (2009) 257–264.
- [32] C. Huang, D. Chen, Y. Lin, R. Ran, Z. Shao, *J. Power Sources* 195 (2010) 5176–5184.
- [33] F. He, T. Wu, R. Peng, C. Xia, *J. Power Sources* 194 (2009) 263–268.
- [34] V.B. Vert, C. Solís, J.M. Serra, *Fuel Cells* 11 (2011) 81–90.
- [35] E. Fabbri, S. Licoccia, E. Traversa, E.D. Wachsmann, *Fuel Cells* 9 (2009) 128–138.
- [36] C. Solís, V.B. Vert, M. Fabuel, J.M. Serra, *J. Power Sources* 196 (2011) 9220–9227.
- [37] K.V. Kravchyk, E. Quarez, C. Solís, J.M. Serra, O. Joubert, *Int. J. Hydrogen Energy* 36 (2011) 13059–13066.